https://doi.org/10.5194/essd-2026-24
Preprint. Discussion started: 27 January 2026

Open Access Earth System Science Data Discussions

GlobalRice20: A 20 m resolution global paddy rice dataset for 2015 and 2024 derived from multi-source remote sensing

Hong Zhang[1,2,3], Mingyang Song[1,2,3*], Yinhaibin Ding[1,2,3], Yazhe Xie[1,2,3], Huadong Guo[1,2,3*], Lu Xu[1,2], Ji Ge[1,2,3], Yafei Zhu[1,2,3], Shenghan Wang[1,2,3], Zihuan Guo[1,2,3], Zhe Wang[1,2,3], Haoxuan Duan[1,2,3], Lijun Zuo[1,2,3], Wenjiang Huang[1,2,3]

[1]Key Laboratory of Digital Earth Science, Aerospace Information Research Institute, Chinese Academy of Sciences, Beijing 100094, China
[2]International Research Center of Big Data for Sustainable Development Goals, Beijing 100094, China
[3]College of Resources and Environment, University of Chinese Academy of Sciences, Beijing 100049, China

Correspondence to: Mingyang Song (songmingyang22@mails.ucas.edu.cn); Huadong Guo (hdguo@radi.ac.cn)

Abstract. Accurate, high-resolution spatial data of paddy rice are indispensable for assessing global food security and tracking progress toward Sustainable Development Goal 2 (Zero Hunger). However, a consistent global rice map at medium-to-high resolution has been lacking due to the challenges of cloud contamination and the temporal irregularity of multi-source satellite archives. Here, we present GlobalRice20, the first global 20m resolution paddy rice dataset for the years 2015 and 2024. We developed a "Time-Series-to-Vision" framework (T2VRCM) that transforms heterogeneous optical and SAR time-series into standardized 2D visual representations, specifically designed to handle irregular sampling and missing modalities. The dataset was produced using Sentinel-1/2 and Landsat imagery and rigorously validated against 164,000 reference samples, achieving an overall accuracy of 92.33%. Cross-comparison with national agricultural statistics reveals a high coefficient of determination (R^2 =0.91 for 2024), confirming the dataset's reliability for national-scale accounting. Spatiotemporal analysis during the first decade of SDGs (2015–2024) indicates a 6.6% expansion in global rice area, with Africa exhibiting the most significant growth (15.7%). This dataset fills a critical gap in global agricultural monitoring, providing a baseline for analyzing food production trends and climate impacts. The dataset is available at https://doi.org/10.5281/zenodo.18168302 (Zhang et al., 2026).

1 Introduction

The year 2025 marks a critical milestone—a decade since the inception of the United Nations Sustainable Development Goals (SDGs). As we approach the 2030 deadline, conducting a rigorous assessment of the progress toward SDG 2 ('Zero Hunger') has become an international priority. Rice, a staple food for billions of people and accounting for over 12% of global cropland area, serves as a key indicator of agricultural sustainability and regional food self-sufficiency (Dong and

https://doi.org/10.5194/essd-2026-24
Preprint. Discussion started: 27 January 2026

Xiao, 2016). However, accurate quantification of rice production landscapes remains a challenge. Reliable, spatially explicit, and high-resolution data are indispensable for evaluating the evolution of planting patterns and formulating targeted interventions. Despite the urgent need to monitor SDG 2 implementation, there is currently a lack of a consistent, high-resolution global monitoring framework capable of capturing the granular evolution of paddy rice from the 2015 baseline to the present.

Currently, the landscape of global rice mapping is characterized by a dichotomy between global low-resolution products and regional high-resolution datasets. At the global scale, prominent datasets—including GDHY (0.5°) (Iizumi and Sakai, 2020), MIRCA2000 (Portmann et al., 2010), M3Crops (Monfreda et al., 2008), and more recent products like GGCP10 (Qin et al., 2024), GlobalCropYield5min (Cao et al., 2025), and GEOGLAM-BACS (Becker-Reshef et al., 2023)—provide valuable long-term trends essential for macro-level yield analysis. However, these coarse-resolution products suffer from mixed-pixel issues that obscure fragmentation and boundary details, lacking the spatial fidelity required for precision agricultural monitoring. In the transition zone, regional products such as MARC (Zhao et al., 2024a), GRIPC (Salmon et al., 2015), and APRA500 (Han et al., 2022) have leveraged MODIS and Sentinel time-series to refine cropping intensity maps. Conversely, at the high-resolution frontier, recent advancements have produced 10–30 m maps using Landsat and Sentinel data. Representative examples include GCD-Rice for Asia (Li et al., 2025b), CCD-Rice for China (Shen et al., 2025), EARice10 for East Asia (Song et al., 2025b), and the 2023 Africa Rice Map (Jiang et al., 2025). By integrating multi-source time-series with machine learning, these efforts have achieved high precision. However, these high-resolution efforts remain largely confined to specific countries or regions. To date, there remains a critical gap: the absence of a unified, validated, and high-resolution (20 m) global rice distribution product that covers major production zones consistently across different years.

With the rapid advancement of remote sensing technology, integrated observation systems have provided a wealth of multi-modal data for agricultural monitoring. Optical imagery (e.g., Landsat series, Sentinel-2, and MODIS) has been widely utilized to capture the unique spectral signatures of rice during key phenological stages, leveraging its rich spectral information (Zhang et al., 2023; Hou et al., 2025; Shen et al., 2024; Ni et al., 2021). However, these sensors are susceptible to cloud and rain interference. In contrast, spaceborne Synthetic Aperture Radar (SAR) offers all-weather and day-and-night observation capabilities, demonstrating unique advantages in rice mapping (Sun et al., 2022; Ge et al., 2025b; Lin et al., 2024; Xu et al., 2023a).

Recently, researchers have significantly enhanced the accuracy and robustness of rice mapping across diverse geographical environments by effectively integrating these optical and SAR data (Shen et al., 2023a; Han et al., 2021; Song et al., 2025a; Wan et al., 2024; Zhao et al., 2024b; Ge et al., 2025a). Methodologically, remote sensing-based rice mapping has evolved through three primary pathways: phenology-based, machine learning, and deep learning methods. Phenology-based approaches utilize specific growth stages; for instance, Xu et al. (2023b) proposed the Sentinel-1-based SPRI index, while Zhao et al. (2024c) developed the "Rice-Sentinel" framework to capture unique flooding signals. Machine learning methods have further improved automation. Liu et al. (2022a) applied Random Forest for early rice mapping, Li et al. (2025a) introduced the SPRC framework integrating phenology with probabilistic voting, and Song et al. (2025b) developed the

https://doi.org/10.5194/essd-2026-24
Preprint. Discussion started: 27 January 2026

SRMI index for optical-SAR fusion. More recently, deep learning has emerged as a dominant paradigm due to its superior non-linear fitting capabilities. Notable examples include the improved U-Net by Wei et al. (2021), the Full-Resolution Network (FR-Net) by Xia et al. (2022), and the lightweight XM-UNet by Ge et al. (2025c) .

Despite these substantial advancements, producing a high-resolution global map faces technical bottlenecks stemming from the heterogeneity of remote sensing archives. Specifically, traditional methods that rely on complex interpolation or temporal aggregation often introduce noise and smooth out critical short-term phenological details (Song et al., 2025a; Yuan et al., 2022b; Blickensdörfer et al., 2022). Furthermore, SAR coverage limitations caused by orbital constraints and imaging modes — exacerbated by the loss of Sentinel-1B — often lead to complete modality missingness, posing a significant challenge for traditional models that rely on the simultaneous availability of optical and SAR observations (Shen et al., 2015; Wei et al., 2022). Most critically, fusing optical and SAR modalities is hindered by temporal asynchrony—the revisit cycles of Landsat, Sentinel-2, and Sentinel-1 do not align, resulting in irregular time-series that traditional models often struggle to handle robustly.

To bridge this gap, we developed the GlobalRice20 dataset, the first globally consistent 20 m resolution paddy rice map for the years 2015 and 2024. To overcome the challenges of irregular sampling and modal missingness, we employed an innovative "Time-series-to-Vision" framework. Unlike conventional methods that require regular time steps, our approach transforms heterogeneous optical and SAR time-series into standardized 2D visual representations, allowing a customized vision model (T2VRCM) to robustly identify rice phenological patterns even in the presence of data gaps. In this study, we present the generation, validation, and analysis of the GlobalRice20 dataset, providing the first verified 20-m resolution global rice map covering 98 major producing countries for 2015 and 2024. By leveraging a novel “Time-series-to-Vision” harmonization strategy to alleviate cloud contamination, sensor asynchrony, and modality missingness, we achieved an overall accuracy of 92.33% and strong agreement with national statistics, supporting the dataset’s reliability and usability at the global scale. Furthermore, we demonstrate the dataset's utility for tracking SDG 2 progress by quantifying critical decadal shifts—such as the 15.7% expansion of rice cultivation in Africa—thereby filling a longstanding gap in high-resolution global agricultural monitoring products.

2 Materials

2.1 Study area

The study covers 98 major rice-producing countries distributed across six continents (Asia, Africa, North America, South America, Europe, and Oceania), encompassing the world’s primary rice cultivation zones as shown in Fig. 1(a). These regions exhibit significant diversity in climatic conditions, topographical features, and cropping systems. According to the Köppen climate classification (Fig. 1(c)), the study area spans Tropical, Arid, Temperate, and Cold zones, with the majority

https://doi.org/10.5194/essd-2026-24
Preprint. Discussion started: 27 January 2026

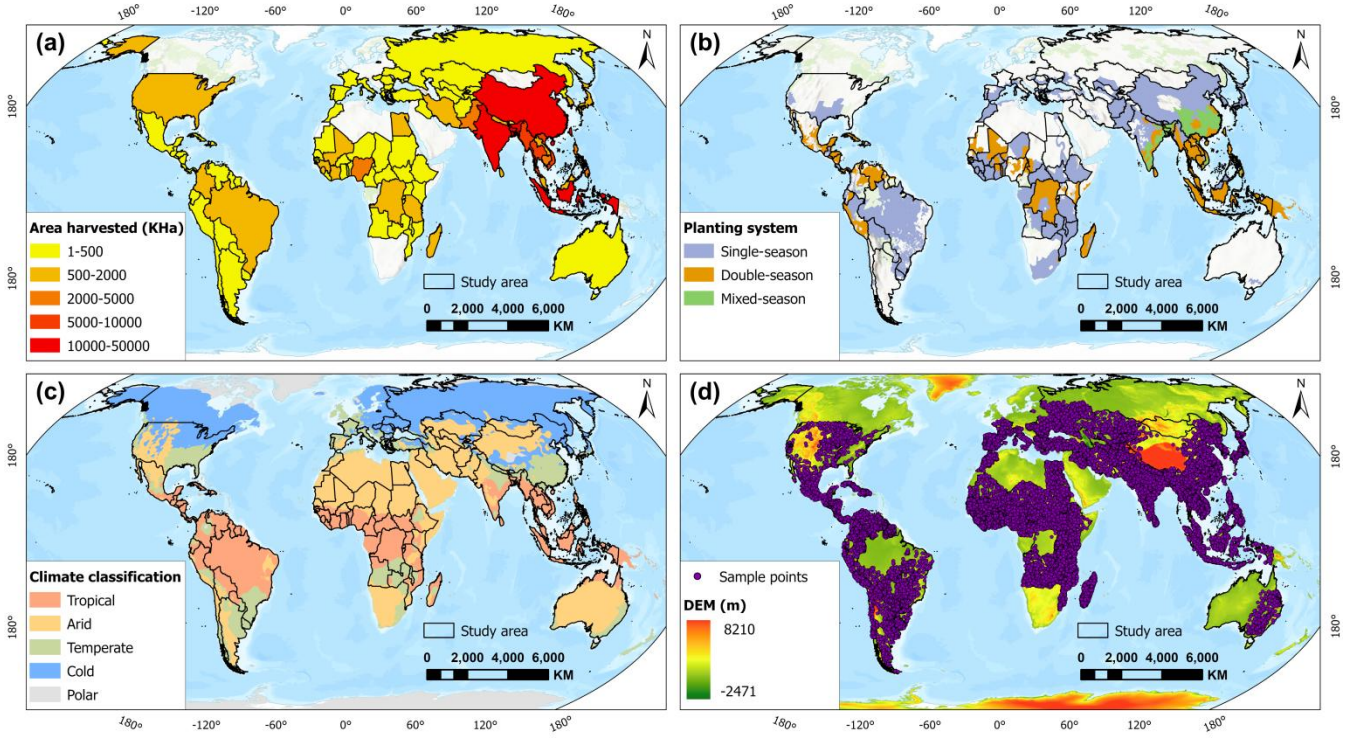

Figure 1. Overview of the study area. (a) Rice planting areas, (b) Rice cropping patterns, (c) Climate zoning, (d) Distribution of validation sample points.

of rice cultivation concentrated in the tropical and subtropical monsoon regions of South and East Asia, which account for over 90% of the global rice sown area (FAOSTAT, 2023).

Rice cropping systems within the study area are categorized into single-season, double-season, and mixed-season regimes, as illustrated in Fig. 1(b) (Laborte et al., 2017). Double-cropping systems are predominantly located in East and Southeast Asia, while single-cropping systems are widely distributed across the Americas, Australia, Europe, and most African nations. This extensive spatial heterogeneity in climate, topography, and cropping intensity poses substantial challenges for producing a consistent high-resolution global paddy rice map.

2.2 Remote Sensing Data

All satellite data processing was conducted on the Google Earth Engine (GEE) cloud computing platform. The primary input datasets consist of multi-temporal Synthetic Aperture Radar (SAR) and optical imagery, selected to correspond with the validation years 2015 and 2024.

For SAR data, we utilized C-band imagery from the Sentinel-1 satellite, which offers all-weather observation capabilities essential for penetrating cloud cover in tropical rice-growing regions. We selected Interferometric Wide (IW) swath mode Ground Range Detected (GRD) products with a 10-m spatial resolution. The data underwent standard preprocessing on GEE,

https://doi.org/10.5194/essd-2026-24
Preprint. Discussion started: 27 January 2026

including thermal noise removal, radiometric calibration, and terrain correction. Because Sentinel-1B was unavailable for the 2015 baseline and ceased operations before 2024, SAR observations for both years rely primarily on Sentinel-1A. Both VV and VH polarizations were utilized, and the SAR acquisitions were aggregated into 12-day mean composites for both 2015 and 2024.

Optical data were sourced from different sensors to maximize spatial resolution and availability for the respective target years. For 2024, we utilized Sentinel-2 MSI Level-2A surface reflectance data (10-m resolution), applying a cloud-masking algorithm to remove invalid observations. For the 2015 target year, as Sentinel-2 data were not yet available, we utilized Landsat-8 OLI surface reflectance data with a 30-m spatial resolution. We calculated the Land Surface Water Index (LSWI) (Xiao et al., 2005) and Enhanced Vegetation Index (EVI) (Huete et al., 1997), widely recognized in optical remote sensing for rice mapping, to characterize the crop's unique phenological evolution.The specific calculation formulas are expressed as follows:

$$\mathrm{LSWI} = \frac{\mathrm{nir} - \mathrm{swir}}{\mathrm{nir} + \mathrm{swir}}$$
$$\mathrm{EVI} = 2.5 * \frac{\mathrm{nir} - \mathrm{red}}{\mathrm{nir} + 6 * \mathrm{red} - 7.5 * \mathrm{blue} + 1} \quad (1)$$

Figure 2 illustrates the resulting spatiotemporal data coverage for these satellite-derived calculations. As shown, Landsat-8 exhibited relatively balanced global coverage in 2015, with slightly fewer observations in northern high-latitude regions. Sentinel-2, due to its high revisit frequency, showed high data coverage globally in 2024. Specifically, in North America, South America, Europe, and Asia, southern regions generally had higher coverage frequencies than northern regions. In Africa, coverage was higher in the north and south but lower in the central region, while Australia exhibited uniformly high coverage frequencies. Regarding SAR data, due to the unavailability of the Sentinel-1B satellite in both 2015 and 2024, coverage was affected but remained robust in key areas. Crucially, the SAR coverage was primarily concentrated in tropical and subtropical regions, effectively compensating for the lack of valid optical observations in these cloud-prone areas.

https://doi.org/10.5194/essd-2026-24
Preprint. Discussion started: 27 January 2026

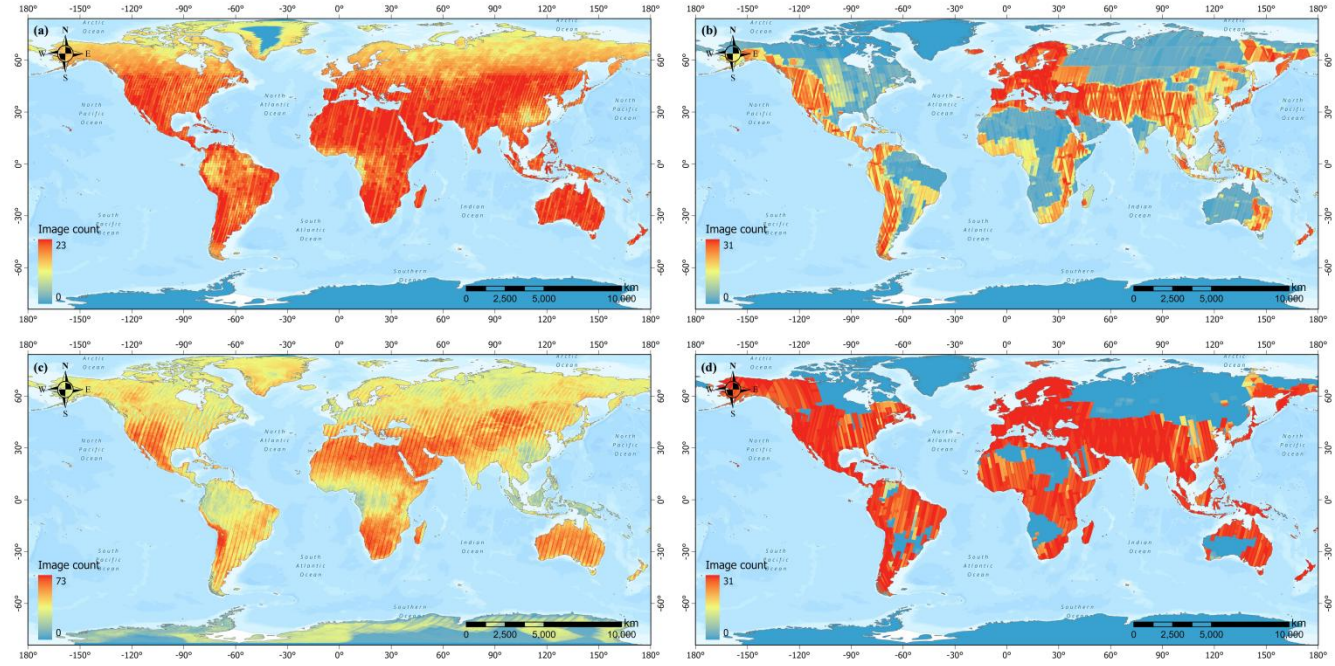

Figure 2. Satellite image coverage frequency in 2015 for (a) Landsat-8 and (b) Sentinel-1, and in 2024 for (c) Sentinel-2 and (d) Sentinel-1.

2.3 Reference and Validation Data

2.3.1 Reference Sample Set

To train and validate the T2VRCM model, a comprehensive reference dataset was constructed containing 164,000 samples across 98 countries. The samples were generated through a rigorous visual interpretation process integrating high-resolution optical imagery and existing regional rice maps. Crucially, to ensure temporal consistency and reduce label noise, we adopted a "stable sample" strategy: selected samples were restricted to locations that maintained a consistent land cover type (either persistent rice or persistent non-rice) in both 2015 and 2024. A balanced 1:1 ratio between rice and non-rice samples was maintained to prevent class imbalance.

2.3.2 Existing Rice Maps and Statistical Data

To assess the quality of the GlobalRice20 dataset, we compiled two types of reference data:

First, we selected 12 representative global and regional datasets for spatial cross-comparison to evaluate geometric accuracy and boundary detail. These include APRA500 (Han et al., 2022), a 500-m product mapping cropping intensity across 21 Asian countries using MODIS data; SingleSeasonRice-China (Shen et al., 2023b), a 10/20-m Sentinel-based dataset covering

https://doi.org/10.5194/essd-2026-24
Preprint. Discussion started: 27 January 2026

21 Chinese provinces; CCD-Rice (Shen et al., 2025), the first long-term (1990–2016) 30-m dataset for China's eastern monsoon region; ChinaCropArea1km (Luo et al., 2020) and SPAM-China (Dai et al., 2025), two 1-km products generated from GLASS LAI and disaggregated statistics, respectively, serving as coarse-resolution baselines; Open-SEA-Rice-10 (Ginting et al., 2025), a recent 10-m map distinguishing triple-cropping systems in Southeast Asia; AsiaRiceYield4km (Wu et al., 2022), a long-term (1995–2015) 4-km gridded product generated via machine learning to estimate seasonal rice yields across Asia; GCD-Rice (Li et al., 2025), a long-term (1990–2023) 30-m dataset mapping seasonal rice distribution across 16 Asian countries using Landsat and Sentinel-1 data; the Japan Historical Rice Map (Carrasco et al., 2022), a long-term (1985–2019) Landsat-based dataset mapping rice field distribution in Japan using phenology and temporal aggregation; the South Korean Dynamic Rice Map (Jo et al., 2023), a dynamic paddy rice mapping product using a Recurrent U-Net deep learning model; NESEA-Rice (Han et al., 2021), a 10-m annual paddy rice dataset covering Northeast and Southeast Asia (2017–2019) developed by integrating Sentinel-1 and MODIS data; and the USDA Cropland Data Layer (Boryan et al., 2011), a 30-m crop land cover product for the United States generated by the USDA using decision-tree classification of satellite imagery. Comparing our results against this diverse set—ranging from 10 m to 4 km and covering both single- and multi-cropping systems—ensures a robust assessment of GlobalRice20's consistency across scales.

Second, to validate the extraction results at a macroscopic level, national-scale rice harvested area statistics for 2015 and 2024 were integrated from two authoritative sources: the United States Department of Agriculture (USDA) and the Food and Agriculture Organization (FAO). These standardized records served as the primary ground truth for assessing the aggregate reliability of our global maps.

3 Methodology

To generate the global 20-m rice map, the comprehensive technical workflow of this study is illustrated in Fig. 3. The core of the methodology lies in the unified encoding of multi-source, heterogeneous remote sensing time-series data—incorporating both SAR and optical observations—into a standardized 2D line-graph visual representation. This visual proxy is subsequently analyzed using a specially designed deep learning vision-based classifier, the T2VRC Model (T2VRCM), to extract sophisticated phenological patterns and achieve high-precision global rice distribution mapping.

https://doi.org/10.5194/essd-2026-24
Preprint. Discussion started: 27 January 2026

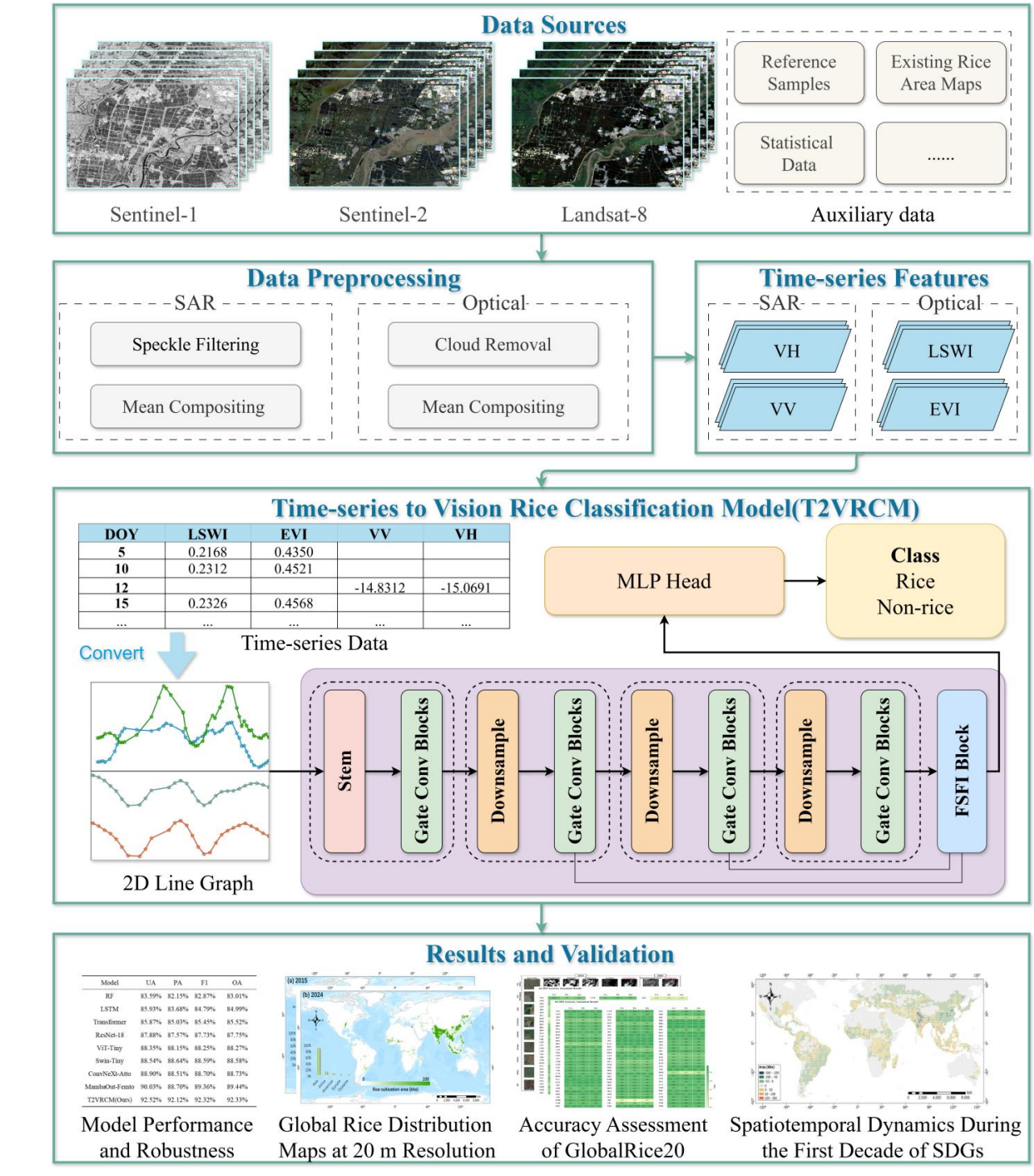

Figure 3. Technical Workflow. Basemap sources: Esri, TomTom, Garmin, FAO, NOAA, USGS, © OpenStreetMap contributors, and the GIS User Community.

https://doi.org/10.5194/essd-2026-24
Preprint. Discussion started: 27 January 2026

3.1 Problem Definition and Notation

The remote sensing data sources used in this study encompass SAR data (Sentinel-1) and optical remote sensing data (Sentinel-2 for 2024, Landsat-8 for 2015). These are integrated with field-collected ground truth sample points to construct a global-scale rice classification dataset. Formally, we define the time series dataset as $\mathcal{D} = \{(S_i, y_i)|i = 1, ..., N\}$, containing N samples. Each sample S_i is associated with a binary label $y_i \in \{0,1\}$, where $y_i = 1$ represents "rice" and $y_i = 0$ represents "non-rice." S_i is a multivariate time series consisting of D variables. In this study, D = 4, corresponding to the optical indices $\{\mathrm{LSWI}, \mathrm{EVI}\}$ and the SAR backscatter coefficients $\{\sigma^0_{VV}, \sigma^0_{VH}\}$. For each variable d, its observations are given by a series of (time, value) tuples: $\left[\left(t_1^d, v_1^d\right), ..., \left(t_{n_d}^d, v_{n_d}^d\right)\right]$, where t represents the observation Day of Year (DOY), and v is the corresponding feature value.

The inherent nature of this dataset is that of an irregularly-sampled time series (Spinnato and Landi, 2025; Weerakody et al., 2021), which is primarily manifested in three aspects：(1) Inconsistent revisit cycles: Different sensors have varying revisit cycles (e.g., 5-day composites for Sentinel-2 and 12-day composites for Sentinel-1); (2)Partial feature missingness: Optical data often suffers from missing observations due to cloud cover, and SAR data may have missing acquisitions during certain periods. (3)Complete modality absence: In some regions, an entire data modality (e.g., SAR) might be completely missing.

Therefore, the research problem is defined as follows: Given this irregular time series dataset $\mathcal{D}$, learn a deep learning model G that can accurately predict the class label $\hat{y}_i \in \{0,1\}$ for each time series sample S_i.

3.2 Time-Series-to-Vision Transformation

To address the challenge of integrating multi-source heterogeneous time-series data, this study proposes an innovative methodology that transforms the time-series classification problem into an image classification problem. By mapping irregularly sampled multimodal time-series data into a standardized two-dimensional image representation, this approach converts challenges such as sensor temporal asynchrony, discontinuous observations, and incomplete data modalities into a visual pattern-recognition task in image space. Consequently, it leverages the powerful feature-extraction capabilities of deep-learning vision models to achieve end-to-end high-precision classification (Ni et al., 2025; Li et al., 2023).

The method adopts a dual-subplot design to explicitly separate and align the optical and SAR modalities. Specifically, the upper subplot displays the two optical features, LSWI and EVI, within the same coordinate system, while the lower subplot plots the two SAR features, σ^0_{VV} and σ^0_{VH}, in a separate coordinate system. In both subplots, the horizontal X-axis represents the Day of Year (DOY, range 1–365), and the vertical Y-axis represents the value of the remote-sensing feature. Only the valid observation points $\left(t_j^d, v_j^d\right)$ for each feature d are connected sequentially by straight lines according to DOY order. This design intuitively represents data missingness: if Sentinel-2 data is absent for a period due to clouds, the line graph directly connects the valid observations before and after the gap; if an entire modality (e.g., Sentinel-1) is completely missing, the corresponding lower subplot remains blank. To enable the model to distinguish between the different lines, four distinct yet consistent colors are assigned to the four features throughout the dataset.

https://doi.org/10.5194/essd-2026-24
Preprint. Discussion started: 27 January 2026

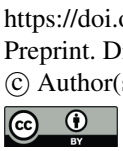

Open Access Earth System Science Data Discussions

Finally, the two subplots are stacked vertically and uniformly resized to a standard RGB image X_i with dimensions 224 × 224 pixels. This "Time-Series-to-Vision" transformation strategy cleverly encodes all heterogeneous, irregular, and incomplete one-dimensional time-series data into a standardized two-dimensional image representation. It systematically addresses critical challenges in multi-source fusion: heterogeneous feature representations, asynchronous acquisitions, intra-series data gaps, and complete modality missingness.

3.3 T2VRCM Visual Classification Model

3.3.1 Overall Architecture

To efficiently analyze the generated 2D time-series graphs, this study proposes the T2VRCM (Time-series to Vision Rice Classification Model), a vision model specifically designed for this classification task. Its overall architecture is shown in Fig. 4. T2VRCM is a hierarchical vision encoder, consisting of four cascaded feature extraction stages (Stages 1–4), a Full-Scale Feature Interaction (FSFI) block, and a Multi-Layer Perceptron (MLP) classification head.

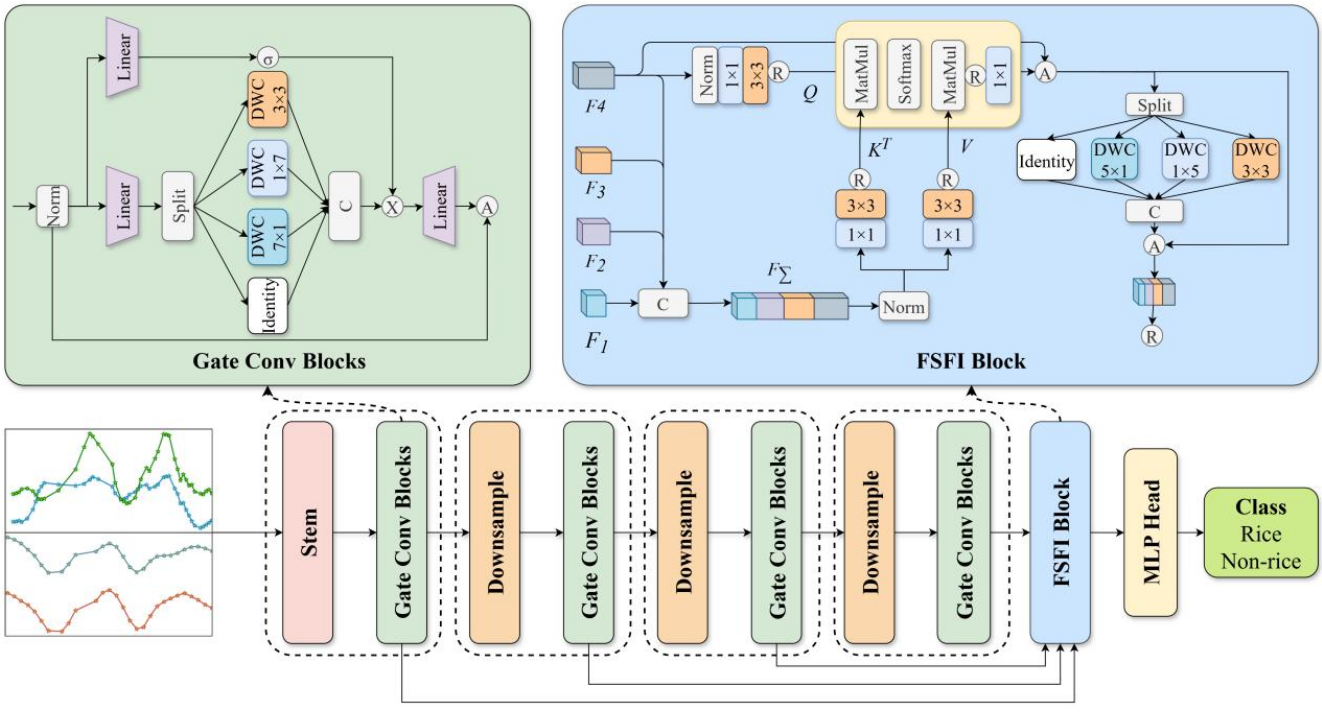

Figure 4. Overall Architecture of T2VRCM

Given an input visual representation $X \in R^{H\times W\times C}$（H = W = 224，C = 3）, its forward propagation process is as follows. X first passes through a Stem layer (composed of two 3×3 convolutions with stride 2), performing 4×downsampling to

https://doi.org/10.5194/essd-2026-24
Preprint. Discussion started: 27 January 2026

Open Access Earth System Science Data Discussions

reduce the resolution to $\frac{H}{4} \times \frac{W}{4}$. The output of the Stem, $S(X)$, is then fed into N_1 stacked Gate Convolution Blocks (G_1), producing the Stage 1 output feature $O_1 = G_1(S(X))$. Each subsequent stage i （$i \in \{2,3,4\}$）consists of a downsampling layer (D_i, a 3×3 convolution with stride 2) and $N_i$stacked G_i blocks, yielding $O_i = G_i(D_i(O_{i-1}))$.

The features $\{O_1, O_2, O_3, O_4\}$ output from the four stages have spatial resolutions of $\frac{H}{4} \times \frac{W}{4}, \frac{H}{8} \times \frac{W}{8}$, $\frac{H}{16} \times \frac{W}{16}, \frac{H}{32} \times \frac{W}{32}$, respectively. They are all fed into the FSFI block to obtain the fused feature F_{fuse}. After processing by Global Average Pooling (GAP) and Layer Normalization (LayerNorm), the final binary logits are produced by the MLP Head, which can be formulated as:

$$\text{Logits} = \text{MLP}\left(\text{LayerNorm}\left(\text{GAP}(F_{fuse})\right)\right) \quad (2)$$

3.3.2 Gate Conv Blocks

The Gate Conv Block is the fundamental feature extraction unit of the T2VRCM encoder (Fig. 4), specifically designed to simultaneously capture local fine-grained patterns and long-range temporal dependencies of rice phenological evolution from the 2D time-series graphs. Its core functionality stems from the synergistic design of a dynamic gating mechanism and Inception-style depthwise separable convolution.

The dynamic gating mechanism adaptively fuses features from two parallel processing paths (the information processing path and the gating path) and incorporates residual connections to facilitate the training of deep networks (Yu and Wang, 2025; Dauphin et al., 2017). Its core role is to perform position-wise adaptive recalibration of features, aiming to amplify discriminative patterns, suppress noise and anomalies, and automatically reduce the contribution of unreliable data sources when modalities are missing or when temporal observations are absent (Dauphin et al., 2017; Yu et al., 2022).

Specifically, given an input feature X, the module first normalizes it to obtain $X' = \text{Norm}(X)$. Its core computation can then be summarized by the following formula:

$$Y = \left(\text{TokenMixer}(X'W_1) \odot \sigma(X'W_2)\right)W_3 + X \quad (3)$$

Here, $X'W_1$ and $X'W_2$ are the linear projections for the information processing path and the gating path, respectively; TokenMixer(·) is the core feature extraction operator; σ(·) is the gating activation function; and ⊙ denotes element-wise multiplication for gating modulation.

In our design, the core feature extraction operator TokenMixer(·) is specifically implemented as an Inception Depthwise Convolution (InceptionDWC) operator (Yu et al., 2024). InceptionDWC is an efficient convolution operator that splits the input channels into four parallel branches: an identity mapping branch, a 3×3 square depthwise convolution branch, and decomposed 1×k and k×1 strip depthwise convolution branches. Its core advantage lies in its ability to simultaneously capture local fine-grained patterns, long-range phenological temporal dependencies, and cross-modal (optical-SAR) feature relationships in the input time-series graph in a computationally efficient manner. Furthermore, this Inception-style multi-

https://doi.org/10.5194/essd-2026-24
Preprint. Discussion started: 27 January 2026

branch design significantly improves computational efficiency while maintaining model accuracy (Yu et al., 2024).

Specifically, for the input $Z=X'W_1$, we split it along the channel dimension into four groups:

$$\begin{aligned} Z_{hw}, Z_w, Z_h, Z_{id} &= \mathrm{Split}(Z) \\ &= Z_{:,:g}, Z_{:,g:2g}, Z_{:,2g:3g}, Z_{:,3g:} \end{aligned} \quad (4)$$

where g is the number of channels per convolution branch. We can set a ratio r_g to determine the branch channel count via $g = r_g C$, where C is the total number of channels in Z. The split inputs are then fed into different parallel branches:

$$\begin{aligned} Z_{hw}' &= \mathrm{DWConv}^{g\to g}_{k_s\times k_s}(Z_{hw}) \\ Z_w' &= \mathrm{DWConv}^{g\to g}_{1\times k_b}(Z_w) \\ Z_h' &= \mathrm{DWConv}^{g\to g}_{k_b\times 1}(Z_h) \\ Z_{id}' &= Z_{id} \end{aligned} \quad (5)$$

Here, k_s denotes the size of the small square convolution kernel (default 3), and k_b denotes the size of the strip convolution kernel (default 7). Finally, the outputs from each branch are concatenated:

$$Z' = \mathrm{Concat}(X_{hw}', X_w', X_h', X_{id}') \quad (6)$$

In summary, the Gate Convolution Block combines the efficient multi-dimensional feature extraction capability of the InceptionDWC operator with the adaptive recalibration function of the dynamic gating mechanism. This enables it to intelligently extract and enhance the most discriminative phenological features from complex 2D time-series graphs while maintaining robustness to data missingness and noise.

3.3.3 FSFI Block

While downsampling operations in the backbone network effectively extract high-dimensional semantic information, the continuously reduced spatial resolution inevitably leads to the loss of crucial fine-grained spatial details. To enhance the model's perception and modeling capabilities for both global and local regions of the line graphs, achieving collaborative interaction across hierarchical features in both channel and spatial dimensions is essential (Yuan et al., 2024a; Song et al., 2025c). For this purpose, we designed the Full-Stage Feature Interaction (FSFI) block, aiming to effectively fuse feature information from different encoder levels, thereby improving the model's classification capability.

Specifically, given the outputs from the four stages as $\{O_1, O_2, O_3, O_4\}$. First, a patch embedding is applied to unify the features from all scales to a common spatial resolution, denoted as $F_i \in R^{C_i\times h\times w}$, where i = 1,2,3,4, h = H/32, and w = W/32. The core of FSFI lies in computing the local-spatial channel similarity between the deepest feature F_4 and features from all levels, thereby establishing global semantic associations. Concretely, the SCA (Spatial Channel Attention) mechanism takes F_4 as the Query, and the concatenated features from all four levels (F_Σ) as the key and value.

FSFI first employs 1×1 convolutions to integrate cross-channel, pixel-wise contextual information, followed by 3×3 depthwise convolutions to capture local spatial context. This process can be formalized as:

https://doi.org/10.5194/essd-2026-24
Preprint. Discussion started: 27 January 2026

$$Q = W_Q^d W_Q^p LN(F_4)$$
$$K = W_K^d W_K^p LN(F_\Sigma) \quad (7)$$
$$V = W_V^d W_V^p LN(F_\Sigma)$$

where $W_Q^d \in R^{C_4\times3\times3}$, $W_Q^p \in R^{C_4\times1\times1}$, $W_K^d \in R^{C_\Sigma\times3\times3}$, $W_K^p \in R^{C_\Sigma\times1\times1}$, $W_V^d \in R^{C_\Sigma\times3\times3}$, $W_V^p \in R^{C_\Sigma\times1\times1}$ are distinct convolution kernels, and LN(·) denotes Layer Normalization.

Subsequently, reshape $Q \in R^{C_4\times h\times w}, K \in R^{C_\Sigma\times h\times w}, V \in R^{C_\Sigma\times h\times w}$ into the forms $R^{C_4\times hw}$, $R^{C_\Sigma\times hw}$, respectively. Then, compute the local spatial-channel similarity using cross-attention:

$$\mathrm{CrossAtt}(Q,K,V) = \mathrm{Softmax}\left\{\frac{Q\,K^T}{\sqrt{C_\Sigma}}\right\}V \quad (8)$$

Next, the output of $\mathrm{CrossAtt}(Q,K,V)$ is reshaped back to $\in R^{C_4\times h\times w}$, restored to the original feature dimension via a 1×1 convolution, and combined with a skip connection to produce $\tilde{F}_4$:

$$\tilde{F}_4 = W_{pi}\,\mathrm{CrossAtt}(Q,K,V) + F_4 \quad (9)$$

To further enhance the model's multi-scale feature representation capability and strengthen its ability to capture key features in the 2D graphs, $\tilde{F}_4$ is fed into another InceptionDWC module (employing 3×3, 1×7, 7×1, and identity mapping branches) for re-enhancement, followed by another residual connection (Yu et al., 2024). The final output of this block, F_{fuse}, is represented as:

$$F_{fuse} = \mathcal{T}_{\mathrm{inceptionDWC}}(\tilde{F}_4) + \tilde{F}_4 \quad (10)$$

In summary, the FSFI Block effectively combines the high-level semantic understanding from the deeper encoder layers with the fine-grained details from the shallower layers, significantly enhancing the model's global and local perception of the 2D time-series graphs. Finally, its highly refined output feature F_{fuse} is fed into a Global Average Pooling layer and the MLP Head to achieve the final high-precision rice/non-rice classification.

3.4 Accuracy Assessment

To comprehensively evaluate model performance, we adopted the following four metrics: Overall Accuracy (OA), Producer's Accuracy for the rice class (PA_{rice}), User's Accuracy for the rice class (UA_{rice}), and the F1 Score. Their specific formulas are as follows:

$$OA = \frac{TP+TN}{TP+TN+FP+FN}$$
$$PA_{rice} = \frac{TP}{TP+FN} \quad (11)$$
$$UA_{rice} = \frac{TP}{TP+FP}$$
$$F1 = 2\times\frac{PA_{rice}\times UA_{rice}}{PA_{rice}+UA_{rice}}$$

where TP, TN, FP, and FN represent True Positives, True Negatives, False Positives, and False Negatives, respectively.

https://doi.org/10.5194/essd-2026-24
Preprint. Discussion started: 27 January 2026


Open Access Earth System Science Data Discussions

3.5 Model Comparison

To validate the effectiveness and superiority of the proposed T2VRCM model and its time-series-to-visualization strategy, this study comprehensively compares T2VRCM with two categories of baseline models. The first category comprises Vision Classification Models, including ResNet-18 (He et al., 2016), ConvNeXt-Atto (Liu et al., 2022b), MambaOut-Femto (Yu and Wang, 2025), ViT-Tiny (Dosovitskiy, 2020), and Swin-Tiny (Liu et al., 2021). These models cover major paradigms from classical Convolutional Neural Networks (CNNs) to modern Transformers. The second category is Native Time-Series Classification Models, commonly used in remote sensing for rice classification. This category includes Random Forest (RF) (Lu et al., 2025) and deep learning models such as Long Short-Term Memory (LSTM) (Hochreiter and Schmidhuber, 1997) and Transformer (Vaswani et al., 2017). To meet these models' prerequisite for regular time-series inputs, we applied corresponding preprocessing strategies: (1) for missing temporal phases, linear interpolation was used to fill gaps; (2) for regions with completely missing single modalities or features that could not be filled via interpolation, values were uniformly set to zero.

Training Configuration and Experimental Environment. To ensure fair comparison, all deep learning models were trained with a unified configuration: the optimizer was AdamW with an initial learning rate of 1e-3 combined with a cosine learning rate decay schedule; batch size was set to 64; and the number of training epochs was uniformly set to 100. All deep learning models were implemented using the PyTorch framework and trained on NVIDIA RTX 3090 GPU.

4. Experimental Results

4.1 Model Performance and Robustness

4.1.1 Comparison Results of Different Models

To validate the proposed strategy, we compared T2VRCM against baseline models on the global dataset (Table 1) . Experimental results demonstrate significant advantages across all metrics.

Among native time-series models, RF showed basic performance (OA=83.01%) due to limited feature extraction capabilities. Deep learning models (LSTM, Transformer) improved accuracy to 84.99% and 85.52% by modeling temporal dependencies but remained significantly lower than vision-based approaches.

Applying the time-series-to-vision strategy enabled all vision models to outperform traditional methods. ResNet-18 achieved an OA of 87.75% (a 2.23% gain over the Transformer), highlighting the efficacy of convolutions in extracting 2D patterns. Modern architectures, such as ViT-Tiny and Swin-Tiny, surpassed an OA of 88%. Notably, MambaOut-Femto emerged as the top performer among the baselines, reaching an OA of 89.44%, largely due to its dynamic gating mechanism which effectively handles noisy graphs.

T2VRCM achieved state-of-the-art performance with an OA of 92.33% and an F1 score of 92.32%, surpassing the best-performing baseline (MambaOut-Femto) by margins of 2.89% and 2.96%, respectively. This stems from three designs: (1)

https://doi.org/10.5194/essd-2026-24
Preprint. Discussion started: 27 January 2026

Inception Depthwise Separable Convolution captures local patterns and cross-modal correlations via multi-branch processing. (2) Dynamic Gating Mechanism adaptively enhances discriminative features while suppressing noise from missing data. (3) Full-Stage Feature Interaction (FSFI) fuses multi-scale features to enhance global-local perception.

In summary, the experimental results validate that the time-series-to-vision strategy effectively elevates the performance of vision-based models above native time-series approaches. Building on this foundation, the proposed T2VRCM achieves the optimal accuracy among all competitors, proving that its specialized visual encoder successfully addresses the critical challenges of multi-source data fusion in global rice classification.

Table 1. Performance Comparison of Different Models

Model	UA	PA	F1	OA
RF	83.59%	82.15%	82.87%	83.01%
LSTM	85.93%	83.68%	84.79%	84.99%
Transformer	85.87%	85.03%	85.45%	85.52%
ResNet-18	87.88%	87.57%	87.73%	87.75%
ViT-Tiny	88.35%	88.15%	88.25%	88.27%
Swin-Tiny	88.54%	88.64%	88.59%	88.58%
ConvNeXt-Atto	88.90%	88.51%	88.70%	88.73%
MambaOut-Femto	90.03%	88.70%	89.36%	89.44%
T2VRCM(Ours)	92.52%	92.12%	92.32%	92.33%

4.1.2 Ablation Experiments

To systematically evaluate the core components of the T2VRCM architecture, we designed ablation experiments. The baseline model was constructed by stacking MambaOut encoding units using standard Depthwise Separable Convolution (DWConv), excluding the Full-Stage Feature Interaction (FSFI) module. Based on this, three variants were tested:(1) Baseline+Inception: Replacing standard DWConv with Inception Depthwise Separable Convolution (InceptionDWC); (2) Baseline+FSFI: Integrating the FSFI module for cross-stage feature fusion; (3) T2VRCM: Integrating both InceptionDWC and FSFI.

Experimental results in Table 2 clearly quantify the contributions of each component. The baseline model yielded an OA of 89.19%. Integrating the InceptionDWC module boosted the performance to an OA of 90.75% (a 1.56% gain), validating the efficacy of multi-branch convolutions in capturing local textures within the 2D graphs. Independently, adding the FSFI module increased the OA to 91.17% (a 1.98% gain), highlighting the crucial role of cross-stage interaction.

The complete T2VRCM achieved peak performance with an OA of 92.33%, marking a substantial total gain of 3.14% over the baseline. This synergy arises because InceptionDWC enriches semantic information, while FSFI further refines fine-

https://doi.org/10.5194/essd-2026-24
Preprint. Discussion started: 27 January 2026

grained discriminative features. Their collaborative interaction allows T2VRCM to fully leverage the representational advantages of the time-series-to-vision strategy.

Table 2. Independent Contributions and Synergistic Gains of Components

Model	UA	PA	F1	OA
T2VRCM	92.52%	92.12%	92.32%	92.33%
Baseline+FSFI	91.32%	90.98%	91.15%	91.17%
Baseline+Inception	91.14%	90.27%	90.71%	90.75%
Baseline	89.95%	88.25%	89.09%	89.19%

4.2 Global Rice Distribution Maps at 20 m Resolution (2015 and 2024)

Based on the proposed T2VRCM, we generated the Global Rice Distribution Maps at 20 m resolution (GlobalRice20). Figure 5 presents the rice cultivation area maps for 2015 and 2024 across 98 rice-producing countries, along with the area proportion statistics for five continents. The maps are displayed aggregated at a 1° grid. Spatially, global rice cultivation areas are widely distributed across Asia, Africa, and the Americas. Asia is the world's primary core rice cultivation region, accounting for nearly 90% of the global total area. Rice cultivation is concentrated in East Asia, South Asia, and Southeast Asia, forming extensive contiguous belts of high-density cultivation. Africa and the Americas are secondary cultivation regions, primarily located in Africa's Nile Delta, coastal West Africa, Madagascar, as well as southern Brazil and the southeastern United States. Cultivation areas in Europe and Oceania are relatively very limited.

https://doi.org/10.5194/essd-2026-24
Preprint. Discussion started: 27 January 2026

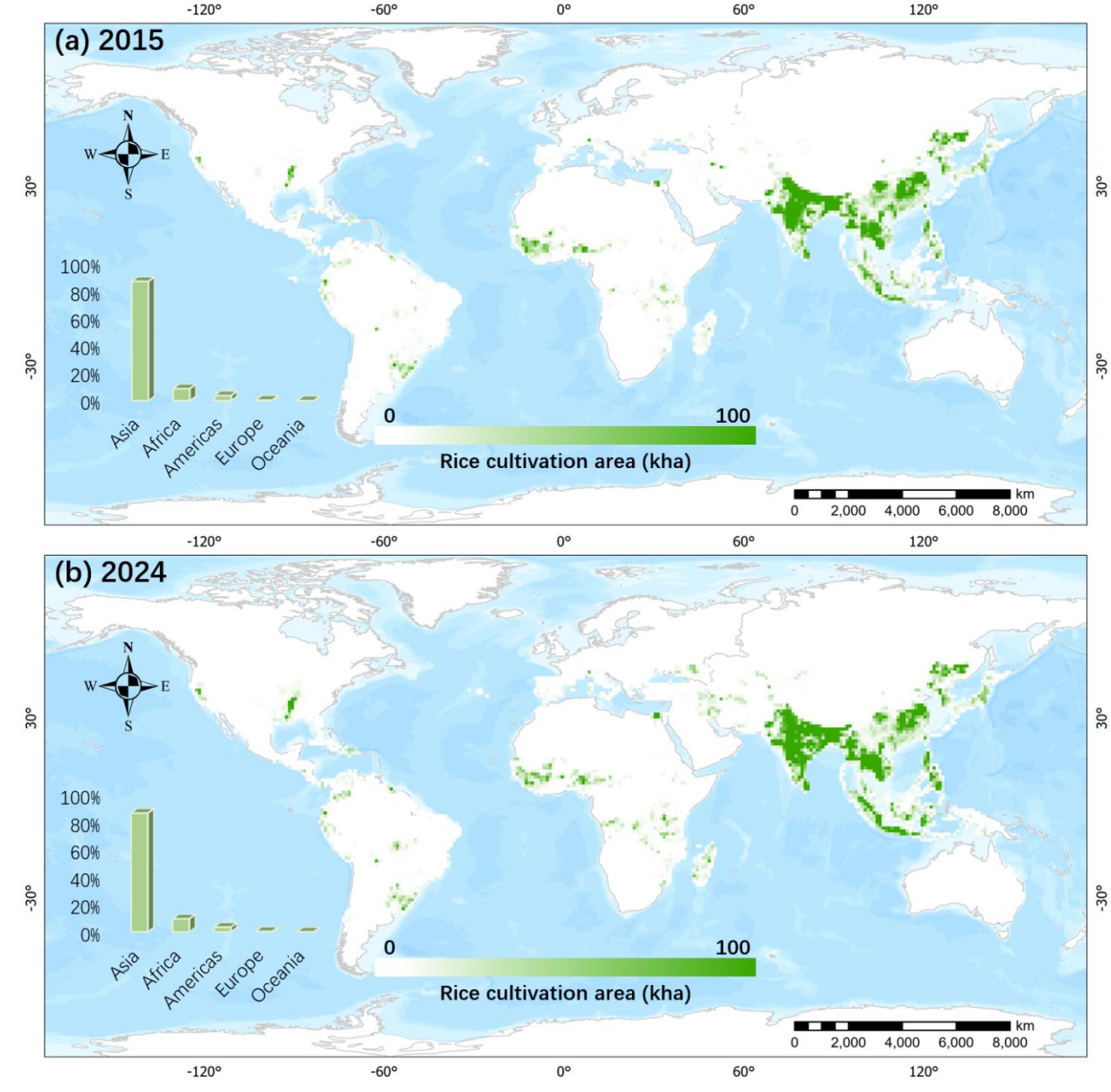

Figure 5. Global spatial distribution maps of rice in 2015 and 2024, along with the proportion of rice cultivation area across five continents. Basemap sources: Esri, TomTom, Garmin, FAO, NOAA, USGS, © OpenStreetMap contributors, and the GIS User Community.

https://doi.org/10.5194/essd-2026-24
Preprint. Discussion started: 27 January 2026

Between 2015 and 2024, the overall pattern of global rice cultivation remained stable, though the proportional contribution of each continent to the total area underwent several shifts; meanwhile, the total global area increased, with Africa emerging as the most significant region in terms of both area expansion and growth in global share.

- Asia: Specifically, Asia consistently dominated rice cultivation, although its share of the total area slightly decreased from 87.15% in 2015 to 86.72% in 2024, yet its absolute area continued to grow from 109,820.4 Kha to 112,948.96 Kha.
- Africa: Africa was the only continent to exhibit a distinct increase in its share of the global total, rising from 8.73% in 2015 to 9.48% in 2024, indicating that rice cultivation in Africa expanded at a faster rate than the global average during the study period; this trend is further reflected in the spatial distribution maps, where rice cultivation areas in Africa in 2024 visually appear denser and more extensive compared to 2015.
- Other Regions: The share for the Americas decreased from 3.69% to 3.45%, while Europe's share dropped from 0.41% to 0.33%, and Oceania maintained the lowest share with negligible change, shifting from 0.02% to 0.03%.

4.3 Accuracy Assessment of GlobalRice20

To strictly assess the quality of the GlobalRice20 product, we conducted a multi-level validation strategy involving ground-truth samples, spatial cross-comparison, and national statistical verification.

4.3.1 Sample-based Validation

We computed accuracy metrics using the independent test set derived from 164,000 global samples (Fig. 6). The global extraction results for 2015 yielded a UA of 90.11%, a PA of 90.36%, and an OA of 90.23%. The corresponding accuracies for 2024 improved to 92.52%, 92.12%, and 92.33%, respectively, demonstrating a clear performance gain over the 2015 baseline.

Furthermore, accuracy was assessed on a country-by-country basis. Among the 2015 mapping results, 84% of countries (83 countries) achieved an OA of 0.85 or higher. In 2024, over 89% of countries (88 countries) achieved an OA of 0.85 or higher. This indicates a high level of consistency between the extracted rice distribution and the independent test samples across diverse regions and observation years.

In Asia, major rice-producing countries such as China, India, Indonesia, and Thailand all achieved overall classification accuracies above 90%. Key rice-producing regions in Africa—Congo, Guinea, Madagascar, and Nigeria—achieved overall accuracies above 85%. Additionally, countries like Brazil in South America and the United States in North America also achieved good accuracy levels.

https://doi.org/10.5194/essd-2026-24
Preprint. Discussion started: 27 January 2026

Open Access Earth System Science Data Discussions

(a) 2015 Accuracy Assessment Results

	UA	PA	OA
AFG	0.94	0.89	0.91
AGO	0.87	0.88	0.88
ARG	0.90	0.92	0.91
AUS	0.82	0.81	0.81
BDI	0.84	0.85	0.84
BEN	0.85	0.86	0.86
BFA	0.88	0.89	0.89
BGD	0.71	0.74	0.72
BGR	0.77	0.77	0.77
BOL	0.90	0.91	0.91
BRA	0.92	0.93	0.92
BRN	0.94	0.90	0.92
BTN	0.93	0.94	0.93
CAF	0.86	0.85	0.86
CHL	0.91	0.92	0.92
CHN	0.90	0.92	0.91
CIV	0.87	0.86	0.87
CMR	0.89	0.90	0.89
COD	0.87	0.86	0.86
COL	0.87	0.83	0.85
CRI	0.83	0.86	0.85
CUB	0.87	0.88	0.87
DOM	0.86	0.85	0.85
ECU	0.93	0.91	0.92
EGY	0.91	0.89	0.90
ESP	0.92	0.92	0.92
ETH	0.87	0.85	0.86
FRA	0.92	0.92	0.92
GHA	0.90	0.89	0.90
GIN	0.82	0.83	0.83
GMB	0.92	0.91	0.91
GNB	0.86	0.91	0.88
GRC	0.92	0.92	0.92

	UA	PA	OA
GTM	0.92	0.94	0.93
GUY	0.85	0.83	0.84
HND	0.93	0.91	0.92
HTI	0.83	0.81	0.82
HUN	0.72	0.66	0.70
IDN	0.77	0.76	0.77
IND	0.87	0.87	0.87
IRN	0.92	0.93	0.92
IRQ	0.92	0.91	0.92
ITA	0.93	0.94	0.94
JPN	0.94	0.94	0.94
KAZ	0.92	0.92	0.92
KEN	0.87	0.87	0.87
KGZ	0.69	0.69	0.69
KHM	0.91	0.91	0.91
LAO	0.92	0.90	0.91
LBR	0.87	0.89	0.88
LKA	0.96	0.95	0.96
MAR	0.90	0.88	0.89
MDG	0.87	0.86	0.86
MEX	0.88	0.87	0.88
MKD	0.92	0.90	0.91
MLI	0.90	0.89	0.90
MMR	0.87	0.87	0.87
MOZ	0.88	0.86	0.87
MRT	0.88	0.90	0.89
MWI	0.94	0.91	0.93
MYS	0.93	0.89	0.91
NER	0.87	0.85	0.86
NGA	0.93	0.94	0.94
NIC	0.83	0.84	0.83
NPL	0.95	0.96	0.96
PAK	0.98	0.99	0.98

	UA	PA	OA
PAN	0.73	0.75	0.74
PER	0.87	0.88	0.88
PHL	0.90	0.91	0.90
PRK	0.93	0.92	0.92
PRK	0.96	0.95	0.96
PRT	0.95	0.95	0.95
PRY	0.89	0.88	0.89
ROU	0.93	0.94	0.93
RUS	0.91	0.91	0.91
RWA	0.89	0.88	0.88
SDN	0.89	0.90	0.90
SEN	0.89	0.87	0.88
SLE	0.81	0.81	0.81
SLV	0.89	0.89	0.89
SSD	0.86	0.85	0.86
SUR	0.85	0.84	0.84
TCD	0.90	0.88	0.89
TGO	0.88	0.89	0.88
THA	0.83	0.83	0.83
TJK	0.92	0.94	0.93
TKM	0.90	0.90	0.90
TLS	0.96	0.96	0.96
TUR	0.92	0.94	0.93
TZA	0.86	0.87	0.86
UGA	0.89	0.90	0.89
UKR	0.92	0.91	0.92
URY	0.92	0.91	0.92
USA	0.91	0.92	0.92
UZB	0.91	0.89	0.90
VEN	0.88	0.88	0.88
VNM	0.92	0.92	0.92
ZMB	0.85	0.87	0.86

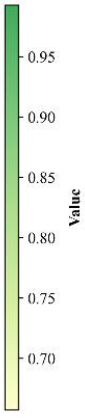

390

https://doi.org/10.5194/essd-2026-24
Preprint. Discussion started: 27 January 2026

(b) 2024 Accuracy Assessment Results

	UA	PA	OA
AFG	0.97	0.95	0.96
AGO	0.88	0.90	0.88
ARG	0.92	0.93	0.93
AUS	0.81	0.80	0.81
BDI	0.89	0.91	0.90
BEN	0.89	0.91	0.90
BFA	0.90	0.89	0.90
BGD	0.94	0.94	0.94
BGR	0.85	0.86	0.85
BOL	0.91	0.93	0.92
BRA	0.92	0.93	0.92
BRN	0.76	0.78	0.77
BTN	0.95	0.93	0.94
CAF	0.90	0.88	0.89
CHL	0.92	0.92	0.92
CHN	0.94	0.93	0.94
CIV	0.89	0.88	0.89
CMR	0.91	0.93	0.92
COD	0.92	0.90	0.91
COL	0.91	0.88	0.90
CRI	0.94	0.92	0.93
CUB	0.92	0.90	0.91
DOM	0.94	0.94	0.94
ECU	0.96	0.95	0.96
EGY	0.95	0.97	0.96
ESP	0.94	0.95	0.94
ETH	0.86	0.88	0.87
FRA	0.97	0.95	0.96
GHA	0.92	0.92	0.92
GIN	0.87	0.90	0.88
GMB	0.93	0.92	0.92
GNB	0.89	0.90	0.89
GRC	0.96	0.95	0.95

	UA	PA	OA
GTM	0.92	0.94	0.93
GUY	0.89	0.87	0.88
HND	0.94	0.95	0.95
HTI	0.96	0.97	0.96
HUN	0.83	0.84	0.83
IDN	0.93	0.92	0.93
IND	0.90	0.91	0.91
IRN	0.91	0.92	0.91
IRQ	0.94	0.96	0.95
ITA	0.96	0.94	0.95
JPN	0.97	0.97	0.97
KAZ	0.95	0.96	0.95
KEN	0.89	0.90	0.90
KGZ	0.80	0.81	0.81
KHM	0.92	0.92	0.92
LAO	0.95	0.94	0.95
LBR	0.89	0.89	0.89
LKA	0.82	0.81	0.82
MAR	0.87	0.88	0.88
MDG	0.90	0.90	0.90
MEX	0.87	0.85	0.86
MKD	0.95	0.95	0.95
MLI	0.90	0.88	0.89
MMR	0.90	0.91	0.90
MOZ	0.89	0.90	0.90
MRT	0.92	0.91	0.91
MWI	0.91	0.90	0.91
MYS	0.93	0.92	0.93
NER	0.89	0.88	0.89
NGA	0.93	0.92	0.92
NIC	0.55	0.50	0.54
NPL	0.82	0.80	0.81
PAK	0.97	0.97	0.97

	UA	PA	OA
PAN	0.88	0.90	0.89
PER	0.92	0.89	0.91
PHL	0.76	0.75	0.75
PRK	0.96	0.96	0.96
PRK	0.97	0.96	0.96
PRT	0.97	0.96	0.97
PRY	0.87	0.85	0.86
ROU	0.95	0.96	0.95
RUS	0.95	0.95	0.95
RWA	0.92	0.91	0.92
SDN	0.89	0.88	0.89
SEN	0.90	0.91	0.90
SLE	0.90	0.85	0.88
SLV	0.92	0.94	0.93
SSD	0.84	0.85	0.84
SUR	0.85	0.84	0.85
TCD	0.87	0.88	0.88
TGO	0.90	0.88	0.89
THA	0.92	0.93	0.93
TJK	0.96	0.95	0.96
TKM	0.71	0.62	0.68
TLS	0.91	0.90	0.91
TUR	0.95	0.93	0.94
TZA	0.90	0.89	0.90
UGA	0.94	0.94	0.94
UKR	0.87	0.87	0.87
URY	0.95	0.92	0.94
USA	0.95	0.94	0.94
UZB	0.90	0.91	0.90
VEN	0.90	0.91	0.91
VNM	0.93	0.93	0.93
ZMB	0.90	0.91	0.90

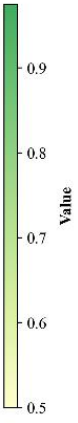

Figure 6. Accuracy validation results based on sample points. (a) Results for 2015. (b) Results for 2024.

4.3.2 Spatial Consistency with Existing Products

Figure 7 presents a spatial comparison between GlobalRice20 and several mainstream rice distribution datasets across nine distinct rice-cultivating regions. For comparative analysis, we selected existing rice maps with varying spatial resolutions that are temporally closest to the target years of 2015 and 2024. With a spatial resolution of 20 m, GlobalRice20 generally surpasses concurrent public regional datasets, thereby meeting the requirements for precise field-level identification.

Taking Anhui and Heilongjiang provinces in China as examples, coarse-resolution datasets such as APRA500, ChinaCropArea1km, AsiaRiceYield4km, and CropArea-China exhibit blurred boundaries and fragmented geometries. Meanwhile, CCD-Rice suffers from excessive noise and significant confusion between large water bodies and paddy fields,

https://doi.org/10.5194/essd-2026-24
Preprint. Discussion started: 27 January 2026

while SingleSeasonRice-China displays substantial noise and misclassification. Consequently, these datasets fail to accurately represent the actual cultivated landscape. Similarly, in regions like Thailand and Indonesia, characterized by fragmented plots and complex cropping structures, other high-resolution datasets (e.g., NESEA-Rice10 and Open-SEA-Rice-10) also exhibit significant data gaps and insufficient delineation of fine details. In contrast, GlobalRice20 clearly delineates field boundaries with regular and well-defined patch contours. It demonstrates high spatial consistency with optical remote sensing imagery, achieving a level of detail comparable to 10-m resolution products.

To further ensure the reliability of the comparison, we validated the accuracy of rice fields in the United States using the USDA NASS Cropland Data Layer (CDL, https://croplandcros.scinet.usda.gov/) for the corresponding years. The results reveal a high spatial agreement between the two, demonstrating the robustness of our dataset across different regions and data standards.

Overall, GlobalRice20 provides a more complete identification scope with clearer contours, effectively and accurately reflecting the spatial distribution of paddy rice fields. Building on this, this study presents the first global 20-m resolution rice classification product covering major rice-growing regions. With its clear boundaries and accurate field delineation, GlobalRice20 fills a critical gap in the availability of high-resolution, timely remote sensing data for global paddy rice monitoring.

https://doi.org/10.5194/essd-2026-24
Preprint. Discussion started: 27 January 2026

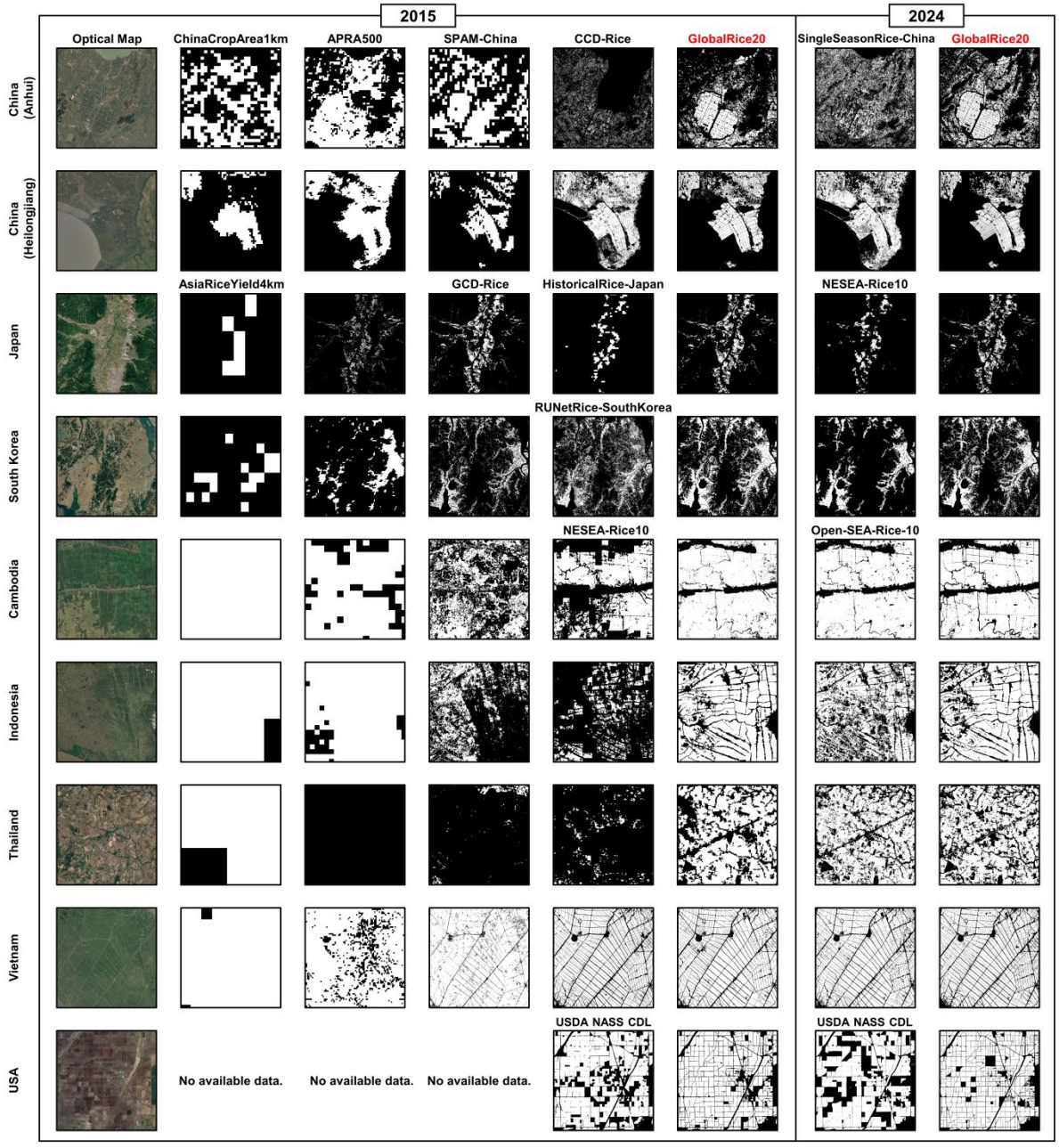

Figure 7. Detailed comparison of our product with existing rice distribution maps. Basemap sources: Esri, TomTom, Garmin, FAO, NOAA, USGS, © OpenStreetMap contributors, and the GIS User Community.

https://doi.org/10.5194/essd-2026-24
Preprint. Discussion started: 27 January 2026

4.3.3 Consistency with Official Statistics

By calculating the predicted rice planting area for each country in 2015 and 2024 and comparing it with statistical data, the results indicate that the estimated areas for both years exhibit a generally high level of consistency with the statistics (Fig. 8). The fit in 2024 is superior, with R^2 of 0.91 between the predicted and statistical areas (Fig. 8b), which is notably higher than that of 0.86 in 2015 (Fig. 8a). The slightly lower accuracy in 2015 can mainly be attributed to the longer revisit cycle of optical imagery and the limited coverage of SAR data in that year, which weakened the representation of time-series image features in some regions and thus affected the stability and accuracy of area estimation, as reflected in the overestimation of rice area in India in 2015. Nevertheless, the 2015 estimates still maintain a good overall fit, demonstrating the robustness of the proposed method under different year-specific and data availability conditions.

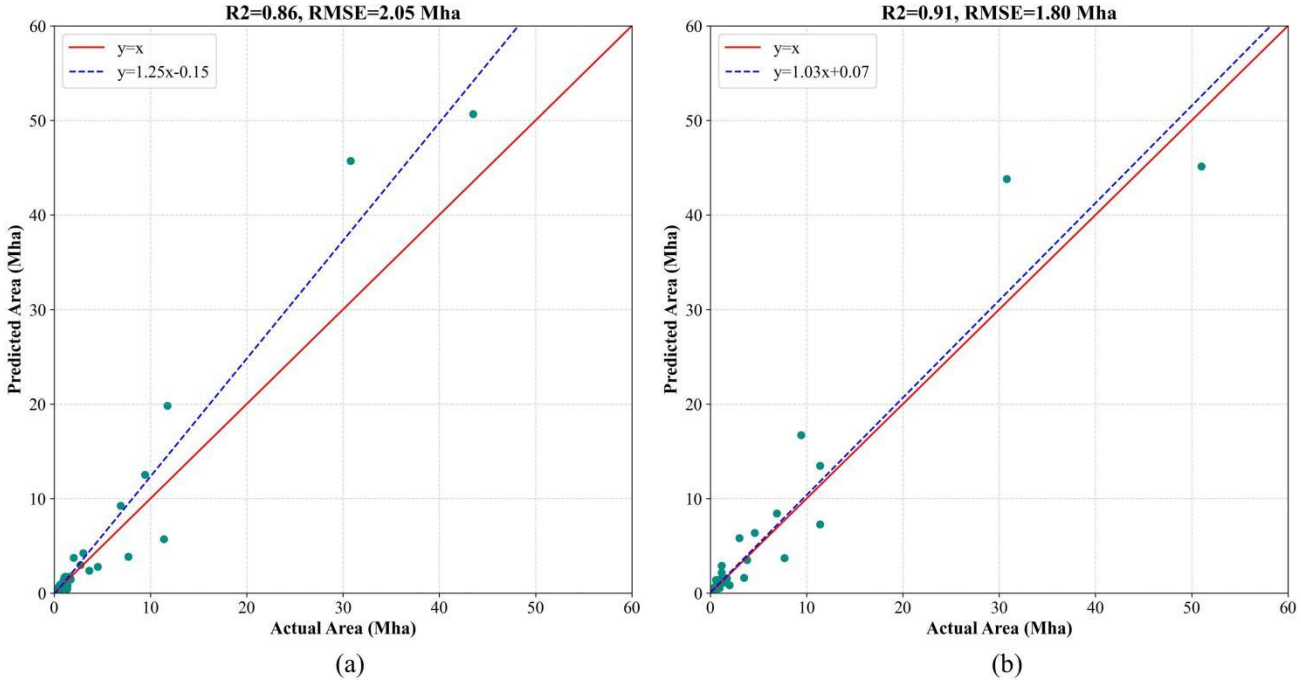

Figure 8. Accuracy validation based on statistical data. (a) R^2 between predicted and statistical rice areas by country in 2015. (b) R^2 between predicted and statistical rice areas by country in 2024.

4.4 Spatiotemporal Dynamics During the First Decade of SDGs (2015–2024)

Global rice area was aggregated into a 1° grid to calculate the area change between 2015 and 2024, as shown in Figure 9. Over this period, the global rice footprint exhibited a robust upward trajectory, registering a net growth of approximately 6.6%. Asia maintained its status as the global center of rice cultivation, though it displayed divergent sub-regional trends. Southeast and South Asia remained the primary drivers of production, benefiting from favorable agro-climatic conditions and abundant water resources (Taniushkina et al., 2024; Yuan et al., 2022a). Specifically, while West Asia and Southeast

https://doi.org/10.5194/essd-2026-24
Preprint. Discussion started: 27 January 2026

Asia saw expansions driven by improved irrigation infrastructure and policy support (Ginting et al., 2025), East and North Asia experienced slight declines, likely attributable to urbanization and cropping structure adjustments. South Asia experienced particularly dramatic fluctuations driven by environmental constraints; for instance, erratic monsoons and groundwater depletion in northwestern India have led to localized field abandonment (Devineni et al., 2022). Conversely, eastern regions of the subcontinent have witnessed expansion supported by government-led irrigation projects, highlighting the complex interplay between climate resilience and policy intervention in this region.

Most notably, Africa emerged as a new global growth pole, recording a substantial 15.7% increase in planting area. This expansion is underpinned by proactive agricultural development policies and international partnerships, such as China-Africa cooperation projects (Zhang et al., 2025). Spatially, a distinct shift in development models was observed across the continent. Traditional producing nations in West Africa (e.g., Nigeria, Senegal) exhibited a pattern of area stabilization or slight decline, reflecting a strategic policy shift towards intensifying yield per unit area to reduce import dependency rather than pursuing further extensive expansion (Yuan et al., 2024b). In contrast, countries in East and Central Africa, such as Uganda, Ethiopia, and Congo, witnessed rapid extensive growth, driven by increased national investments in new paddy field development and irrigation infrastructure.

Looking ahead, Africa's rice production trajectory is poised for continued ascent. Driven by technology dissemination and infrastructure modernization, the continent is gradually building a resilient and mature value chain. With advancements in irrigation systems, seed varieties, and mechanization, Africa has the potential to significantly boost its self-sufficiency rates in the coming decades, providing crucial support for regional food security and the realization of SDG 2.

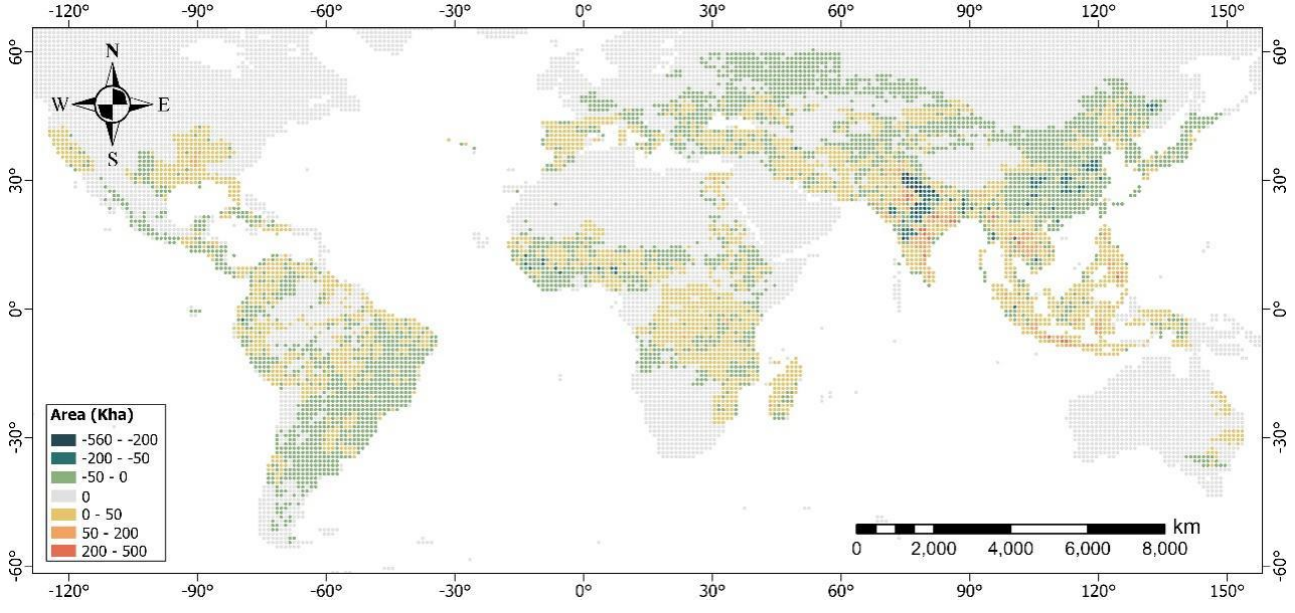

Figure 9. Spatiotemporal statistics of global rice area change aggregated at a 1° grid over the decade (2015–2024).

https://doi.org/10.5194/essd-2026-24
Preprint. Discussion started: 27 January 2026

5. Conclusion

To address the persistent challenges of fusing multi-source time-series remote sensing data for global-scale agricultural monitoring, this study proposes an innovative "Time-Series-to-Vision" classification framework and develops a specialized deep learning visual classifier, T2VRCM. By leveraging the complementary strengths of multi-source remote sensing data, we successfully generated GlobalRice20, the first validated global 20-m resolution rice distribution product for the years 2015 and 2024. The core innovation of this study lies in encoding heterogeneous, irregularly sampled Optical and SAR time-series data into standardized 2D line-graph visual representations. This strategy effectively resolves critical technical bottlenecks—specifically sensor asynchrony, temporal discontinuity, and modal missingness—enabling high-precision, end-to-end rice mapping even in complex, cloud-prone environments. Experimental results demonstrate that the proposed T2VRCM achieves an OA of 92.33% across 98 countries, significantly outperforming existing state-of-the-art native time-series models and general vision classifiers. The generated global maps exhibit high spatial consistency and statistical reliability, confirmed through rigorous validation against both ground-truth samples and official national statistics, yielding a high correlation ($R^2 = 0.91$) for 2024. Based on this high-resolution dataset, we systematically analyzed the spatiotemporal evolution of global rice cultivation over the decade following the inception of SDG 2. The analysis reveals an overall growth of approximately 6.6% in the total global rice area. Notably, a pivotal geographical shift was observed: Africa emerged as the most significant growth hotspot with a 15.7% expansion, contrasting with the relative stability of traditional Asian production hubs, where the total share has slightly decreased. In conclusion, the high-resolution, multi-temporal rice distribution dataset constructed in this study fills a critical gap in global-scale thematic products. By providing spatially explicit and timely benchmarks, GlobalRice20 offers essential data support for global food security assessment, agricultural policy formulation, and tracking progress toward Sustainable Development Goal 2 (Zero Hunger) in the face of climate change.

Author Contributions: Conceptualization, H.Z., M.S., H.G., L.Z. and W.H.; methodology, M.S., H.Z. and H.G.; software, M.S., Y.D., Y.X, Z.W. and H.D.; validation, J.G., Y.Z., S.W. and Z.G.; formal analysis, M.S., H.Z. and H.G.; investigation, M.S. and H.Z.; resources, H.G., W.H., L.Z. and L.X.; data curation, M.S., L.X., Y.D. and Y.X.; writing—original draft preparation, H.Z., M.S., Y.D, and Y.X.; writing—review and editing, H.G., W.H., L.Z., L.X., H.Z. and J.G.; visualization, Y.D., Y.X., Z.W. and H.D.; supervision, H.G., W.H., L.Z., L.X. and H.Z.; project administration, H.G., W.H., L.Z. and H.Z. All authors have read and agreed to the published version of the manuscript.

Funding: This research was supported by the International Research Center of Big Data for Sustainable Development Goals (CBAS) (No. CBASYX0906) and the National Key R&D Program of China (No. 2023YFB3906201).

Acknowledgments: The authors acknowledge the support of data and computational power provided by the Google Earth Engine platform.

Competing interests: The authors declare no conflict of interest.

https://doi.org/10.5194/essd-2026-24
Preprint. Discussion started: 27 January 2026

Open Access Earth System Science Data Discussions

Data availability: The GlobalRice20 dataset is available at https://doi.org/10.5281/zenodo.18168302 (Zhang et al., 2026).

References

Becker-Reshef, I., Barker, B., Whitcraft, A., Oliva, P., Mobley, K., Justice, C., and Sahajpal, R.: Crop type maps for operational global agricultural monitoring, Scientific Data, 10, 172, 2023.

Blickensdörfer, L., Schwieder, M., Pflugmacher, D., Nendel, C., Erasmi, S., and Hostert, P.: Mapping of crop types and crop sequences with combined time series of Sentinel-1, Sentinel-2 and Landsat 8 data for Germany, Remote sensing of environment, 269, 112831, 2022.

Boryan, C., Yang, Z., Mueller, R., and Craig, M.: Monitoring US agriculture: the US department of agriculture, national agricultural statistics service, cropland data layer program, Geocarto International, 26, 341-358, 2011.

Cao, J., Zhang, Z., Luo, X., Luo, Y., Xu, J., Xie, J., Han, J., and Tao, F.: Mapping global yields of four major crops at 5-minute resolution from 1982 to 2015 using multi-source data and machine learning, Scientific Data, 12, 357, 2025.

Carrasco, L., Fujita, G., Kito, K., and Miyashita, T.: Historical mapping of rice fields in Japan using phenology and temporally aggregated Landsat images in Google Earth Engine, ISPRS Journal of Photogrammetry and Remote Sensing, 191, 277-289, 2022.

Dai, K., Cheng, C., Li, B., Xie, Y., Gomez, J. A., Wang, Z., and Wu, X.: Mapping the harvest area of a comprehensive set of crop types in China from 1990 to 2020 at a 1-km resolution, Scientific Data, 12, 1371, 2025.

Dauphin, Y. N., Fan, A., Auli, M., and Grangier, D.: Language modeling with gated convolutional networks, International conference on machine learning, 933-941,

Devineni, N., Perveen, S., and Lall, U.: Solving groundwater depletion in India while achieving food security, Nature Communications, 13, 3374, 2022.

Dong, J. and Xiao, X.: Evolution of regional to global paddy rice mapping methods: A review, ISPRS Journal of Photogrammetry and Remote Sensing, 119, 214-227, 2016.

Dosovitskiy, A.: An image is worth 16x16 words: Transformers for image recognition at scale, arXiv preprint arXiv:2010.11929, 2020.

FAOSTAT: World food and agriculture–statistical yearbook 2023, World Food and Agriculture–Statistical Yearbook 2023, 2023.

Ge, J., Zhang, H., Huang, W., Guo, Z., Xu, L., Xie, Y., Song, M., Ding, Y., and Wang, C.: Plot-Rice v1. 0: A global plot-based rice benchmark dataset with spatiotemporal heterogeneity for scientific deep learning, International Journal of Applied Earth Observation and Geoinformation, 140, 104569, 2025a.

Ge, J., Zhang, H., Zuo, L., Xu, L., Jiang, J., Song, M., Ding, Y., Xie, Y., Wu, F., and Wang, C.: Large-scale rice mapping under spatiotemporal heterogeneity using multi-temporal SAR images and explainable deep learning, ISPRS Journal of Photogrammetry and Remote Sensing, 220, 395-412, 2025b.

https://doi.org/10.5194/essd-2026-24
Preprint. Discussion started: 27 January 2026

Ginting, F. I., Rudiyanto, R., Fatchurrachman, Mohd Shah, R., Che Soh, N., Eng Giap, S. G., Fiantis, D., Setiawan, B. I., Schiller, S., and Davitt, A.: High-resolution maps of rice cropping intensity across Southeast Asia, Scientific Data, 12, 1408, 2025.

Han, J., Zhang, Z., Luo, Y., Cao, J., Zhang, L., Cheng, F., Zhuang, H., Zhang, J., and Tao, F.: NESEA-Rice10: high-resolution annual paddy rice maps for Northeast and Southeast Asia from 2017 to 2019, Earth system science data, 13, 5969-5986, 2021.

Han, J., Zhang, Z., Luo, Y., Cao, J., Zhang, L., Zhuang, H., Cheng, F., Zhang, J., and Tao, F.: Annual paddy rice planting area and cropping intensity datasets and their dynamics in the Asian monsoon region from 2000 to 2020, Agricultural Systems, 200, 103437, 2022.

He, K., Zhang, X., Ren, S., and Sun, J.: Deep residual learning for image recognition, Proceedings of the IEEE conference on computer vision and pattern recognition, 770-778,

Hochreiter, S. and Schmidhuber, J.: Long short-term memory, Neural computation, 9, 1735-1780, 1997.

Hou, D., Chen, J., Dong, J., Ji, C., Feng, J., Du, G., and Yang, L.: A 30-m annual paddy rice dataset in Northeastern China during period 2000–2023, Scientific Data, 12, 1355, 2025.

Hu, J., Chen, Y., Cai, Z., Wei, H., Zhang, X., Zhou, W., Wang, C., You, L., and Xu, B.: Mapping diverse paddy rice cropping patterns in South China using harmonized Landsat and Sentinel-2 data, Remote Sensing, 15, 1034, 2023.

Huete, A., Liu, H., Batchily, K., and Van Leeuwen, W.: A comparison of vegetation indices over a global set of TM images for EOS-MODIS, Remote sensing of environment, 59, 440-451, 1997.

Iizumi, T. and Sakai, T.: The global dataset of historical yields for major crops 1981–2016, Scientific Data, 7, 97, 2020.

Jiang, J., Zhang, H., Ge, J., Zuo, L., Xu, L., Song, M., Ding, Y., Xie, Y., and Huang, W.: The 20 m Africa rice distribution map of 2023, Earth System Science Data, 17, 1781-1805, 2025.

Jo, H.-W., Park, E., Sitokonstantinou, V., Kim, J., Lee, S., Koukos, A., and Lee, W.-K.: Recurrent U-Net based dynamic paddy rice mapping in South Korea with enhanced data compatibility to support agricultural decision making, GIScience & Remote Sensing, 60, 2206539, 2023.

Karimi, N. and Torabi, O.: Remote Sensing-Based Bathymetry Mapping in Shallow Lakes: Comparative Analysis of Sentinel-2 and Landsat-8 Imagery Integrated with Machine Learning Techniques, Advances in Space Research, 2025.

Laborte, A. G., Gutierrez, M. A., Balanza, J. G., Saito, K., Zwart, S. J., Boschetti, M., Murty, M., Villano, L., Aunario, J. K., and Reinke, R.: RiceAtlas, a spatial database of global rice calendars and production, Scientific data, 4, 1-10, 2017.

Li, J., Xue, F., Li, G., Zhang, M., Tian, J., and Zhang, H.: SPRC: A novel Sentinel-1/-2 Phenology-enhanced framework for automated paddy rice mapping, International Journal of Applied Earth Observation and Geoinformation, 143, 104772, 2025a.

Li, S., Shen, R., Jiang, J., Peng, Q., Chen, X., Dong, J., Dong, J., and Yuan, W.: A long-term paddy rice distribution dataset in Asia at a 30 m spatial resolution, Scientific Data, 12, 1052, 2025b.

https://doi.org/10.5194/essd-2026-24
Preprint. Discussion started: 27 January 2026

555 Li, Z., Li, S., and Yan, X.: Time series as images: Vision transformer for irregularly sampled time series, Advances in Neural Information Processing Systems, 36, 49187-49204, 2023.

Lin, S., Qi, Z., Li, X., Zhang, H., Lv, Q., and Huang, D.: A phenological-knowledge-independent method for automatic paddy rice mapping with time series of polarimetric SAR images, ISPRS Journal of Photogrammetry and Remote Sensing, 218, 628-644, 2024.

560 Liu, Y., Xiao, D., and Yang, W.: An algorithm for early rice area mapping from satellite remote sensing data in southwestern Guangdong in China based on feature optimization and random Forest, Ecological informatics, 72, 101853, 2022a.

Liu, Z., Mao, H., Wu, C.-Y., Feichtenhofer, C., Darrell, T., and Xie, S.: A convnet for the 2020s, Proceedings of the IEEE/CVF conference on computer vision and pattern recognition, 11976-11986,

Liu, Z., Lin, Y., Cao, Y., Hu, H., Wei, Y., Zhang, Z., Lin, S., and Guo, B.: Swin transformer: Hierarchical vision transformer
565 using shifted windows, Proceedings of the IEEE/CVF international conference on computer vision, 10012-10022,

Lu, C., Xu, H., Yao, Q., Liu, Q., Bricker, J. D., Jonkman, S. N., Yin, J., and Wang, J.: Tracking 30-year evolution of subsidence in Shanghai utilizing multi-sensor InSAR and random forest modelling, International Journal of Applied Earth Observation and Geoinformation, 140, 104606, 2025.

Luo, Y., Zhang, Z., Li, Z., Chen, Y., Zhang, L., Cao, J., and Tao, F.: Identifying the spatiotemporal changes of annual
570 harvesting areas for three staple crops in China by integrating multi-data sources, Environmental Research Letters, 15, 074003, 2020.

Maze, M., Attaher, S., Taqi, M. O., Elsawy, R., El-Moula, M. M. G., Hashem, F. A., and Moussa, A. S.: Enhanced agricultural land use/land cover classification in the Nile Delta using Sentinel-1 and Sentinel-2 data and machine learning, ISPRS Journal of Photogrammetry and Remote Sensing, 229, 239-253, 2025.

575 Monfreda, C., Ramankutty, N., and Foley, J. A.: Farming the planet: 2. Geographic distribution of crop areas, yields, physiological types, and net primary production in the year 2000, Global biogeochemical cycles, 22, 2008.

Mullissa, A., Vollrath, A., Odongo-Braun, C., Slagter, B., Balling, J., Gou, Y., Gorelick, N., and Reiche, J.: Sentinel-1 sar backscatter analysis ready data preparation in google earth engine, Remote Sensing, 13, 1954, 2021.

Ni, J., Zhao, Z., Shen, C., Tong, H., Song, D., Cheng, W., Luo, D., and Chen, H.: Harnessing vision models for time series
580 analysis: A survey, arXiv preprint arXiv:2502.08869, 2025.

Ni, R., Tian, J., Li, X., Yin, D., Li, J., Gong, H., Zhang, J., Zhu, L., and Wu, D.: An enhanced pixel-based phenological feature for accurate paddy rice mapping with Sentinel-2 imagery in Google Earth Engine, ISPRS Journal of Photogrammetry and Remote Sensing, 178, 282-296, 2021.

Ni, R., Tian, J., Li, X., Yin, D., Li, J., Gong, H., Zhang, J., Zhu, L., and Wu, D.: An enhanced pixel-based phenological
585 feature for accurate paddy rice mapping with Sentinel-2 imagery in Google Earth Engine, ISPRS Journal of Photogrammetry and Remote Sensing, 178, 282-296, 2021.

https://doi.org/10.5194/essd-2026-24
Preprint. Discussion started: 27 January 2026

Portmann, F. T., Siebert, S., and Döll, P.: MIRCA2000—Global monthly irrigated and rainfed crop areas around the year 2000: A new high - resolution data set for agricultural and hydrological modeling, Global biogeochemical cycles, 24, 2010.

Qin, X., Wu, B., Zeng, H., Zhang, M., and Tian, F.: Global gridded crop production dataset at 10 km resolution from 2010 to 2020, Scientific Data, 11, 1377, 2024.

Salmon, J. M., Friedl, M. A., Frolking, S., Wisser, D., and Douglas, E. M.: Global rain-fed, irrigated, and paddy croplands: A new high resolution map derived from remote sensing, crop inventories and climate data, International Journal of Applied Earth Observation and Geoinformation, 38, 321-334, 2015.

Shen, H., Li, X., Cheng, Q., Zeng, C., Yang, G., Li, H., and Zhang, L.: Missing information reconstruction of remote sensing data: A technical review, IEEE Geoscience and Remote Sensing Magazine, 3, 61-85, 2015.

Shen, R., Peng, Q., Li, X., Chen, X., and Yuan, W.: CCD-Rice: A long-term paddy rice distribution dataset in China at 30 m resolution, Earth System Science Data Discussions, 2024, 1-33, 2024.

Shen, R., Pan, B., Peng, Q., Dong, J., Chen, X., Zhang, X., Ye, T., Huang, J., and Yuan, W.: High-resolution distribution maps of single-season rice in China from 2017 to 2022, Earth System Science Data Discussions, 2023, 1-27, 2023.

Song, M., Xu, L., Zhu, N., Guo, Z., Duan, H., Teng, J., Lei, X., and Zuo, L.: A Fine Agricultural Flood Segmentation Model for HJ-2E S-Band SAR Data, IEEE Journal of Selected Topics in Applied Earth Observations and Remote Sensing, 2025a.

Song, M., Xu, L., Ge, J., Zhang, H., Zuo, L., Jiang, J., Ding, Y., Xie, Y., and Wu, F.: EARice10: a 10 m resolution annual rice distribution map of East Asia for 2023, Earth system science data, 17, 661-683, 2025b.

Spinnato, F. and Landi, C.: PYRREGULAR: A Unified Framework for Irregular Time Series, with Classification Benchmarks, arXiv preprint arXiv:2505.06047, 2025.

Sun, C., Zhang, H., Xu, L., Ge, J., Jiang, J., Zuo, L., and Wang, C.: 20 m Annual Paddy Rice Map for Mainland Southeast Asia Using Sentinel-1 SAR Data, Earth System Science Data Discussions, 2022, 1-25, 2022.

Taniushkina, D., Lukashevich, A., Shevchenko, V., Belalov, I. S., Sotiriadi, N., Narozhnaia, V., Kovalev, K., Krenke, A., Lazarichev, N., and Bulkin, A.: Case study on climate change effects and food security in Southeast Asia, Scientific Reports, 14, 16150, 2024.

Vaswani, A., Shazeer, N., Parmar, N., Uszkoreit, J., Jones, L., Gomez, A. N., Kaiser, Ł., and Polosukhin, I.: Attention is all you need, Advances in neural information processing systems, 30, 2017.

Wan, Y., Gong, Y., Xu, F., Shi, W., and Gao, W.: A novel red-edge vegetable index for paddy rice mapping based on Sentinel-1/2 and GF-6 images, International Journal of Digital Earth, 17, 2398068, 2024.

Weerakody, P. B., Wong, K. W., Wang, G., and Ela, W.: A review of irregular time series data handling with gated recurrent neural networks, Neurocomputing, 441, 161-178, 2021.

https://doi.org/10.5194/essd-2026-24
Preprint. Discussion started: 27 January 2026

Wei, P., Chai, D., Lin, T., Tang, C., Du, M., and Huang, J.: Large-scale rice mapping under different years based on time-series Sentinel-1 images using deep semantic segmentation model, ISPRS journal of photogrammetry and remote sensing, 174, 198-214, 2021.

Wei, P., Chai, D., Huang, R., Peng, D., Lin, T., Sha, J., Sun, W., and Huang, J.: Rice mapping based on Sentinel-1 images using the coupling of prior knowledge and deep semantic segmentation network: A case study in Northeast China from 2019 to 2021, International Journal of Applied Earth Observation and Geoinformation, 112, 102948, 2022.

Wu, H., Zhang, J., Zhang, Z., Han, J., Cao, J., Zhang, L., Luo, Y., Mei, Q., Xu, J., and Tao, F.: AsiaRiceYield4km: seasonal rice yield in Asia from 1995 to 2015, Earth System Science Data Discussions, 2022, 1-30, 2022.

Xia, L., Zhao, F., Chen, J., Yu, L., Lu, M., Yu, Q., Liang, S., Fan, L., Sun, X., and Wu, S.: A full resolution deep learning network for paddy rice mapping using Landsat data, ISPRS Journal of Photogrammetry and Remote Sensing, 194, 91-107, 2022.

Xiao, X., Boles, S., Frolking, S., Salas, W., Moore Iii, B., Li, C., He, L., and Zhao, R.: Observation of flooding and rice transplanting of paddy rice fields at the site to landscape scales in China using VEGETATION sensor data, International Journal of Remote Sensing, 23, 3009-3022, 2002.

Xu, S., Zhu, X., Chen, J., Zhu, X., Duan, M., Qiu, B., Wan, L., Tan, X., Xu, Y. N., and Cao, R.: A robust index to extract paddy fields in cloudy regions from SAR time series, Remote Sensing of Environment, 285, 113374, 2023.

Yu, W. and Wang, X.: Mambaout: Do we really need mamba for vision?, Proceedings of the Computer Vision and Pattern Recognition Conference, 4484-4496,

Yu, W., Zhou, P., Yan, S., and Wang, X.: Inceptionnext: When inception meets convnext, Proceedings of the IEEE/cvf conference on computer vision and pattern recognition, 5672-5683,

Yu, W., Luo, M., Zhou, P., Si, C., Zhou, Y., Wang, X., Feng, J., and Yan, S.: Metaformer is actually what you need for vision, Proceedings of the IEEE/CVF conference on computer vision and pattern recognition, 10819-10829,

Yu, W., Xiong, Y., Li, X., Zheng, H., Jiang, C., Yao, X., Zhu, Y., Cao, W., Qiu, L., and Song, L.: Rice yield prediction in unseen years at field level with high-resolution gross primary productivity derived from Sentinel-2 imagery, Remote Sensing of Environment, 332, 115061, 2026.

Yuan, S., Qin, H., Yan, X., Akhtar, N., and Mian, A.: Sctransnet: Spatial-channel cross transformer network for infrared small target detection, IEEE Transactions on Geoscience and Remote Sensing, 62, 1-15, 2024a.

Yuan, S., Saito, K., van Oort, P. A., van Ittersum, M. K., Peng, S., and Grassini, P.: Intensifying rice production to reduce imports and land conversion in Africa, Nature communications, 15, 835, 2024b.

Yuan, S., Stuart, A. M., Laborte, A. G., Rattalino Edreira, J. I., Dobermann, A., Kien, L. V. N., Thúy, L. T., Paothong, K., Traesang, P., and Tint, K. M.: Southeast Asia must narrow down the yield gap to continue to be a major rice bowl, Nature Food, 3, 217-226, 2022a.

https://doi.org/10.5194/essd-2026-24
Preprint. Discussion started: 27 January 2026

Yuan, Y., Lin, L., Liu, Q., Hang, R., and Zhou, Z.-G.: SITS-Former: A pre-trained spatio-spectral-temporal representation model for Sentinel-2 time series classification, International Journal of Applied Earth Observation and Geoinformation, 106, 102651, 2022b.

Zhang, C., Zhang, H., and Tian, S.: Phenology-assisted supervised paddy rice mapping with the Landsat imagery on Google Earth Engine: Experiments in Heilongjiang Province of China from 1990 to 2020, Computers and Electronics in Agriculture, 212, 108105, 2023.

Zhang, D., Lin, Q., Stephen, O. T., and Mao, S.: Assessing the Effects of China's Rice Technology Transfer to Africa: Economic and Environmental Impacts on Rice Production, Food and Energy Security, 14, e70146, 2025.

Zhang, H., Song, M., Ding, Y., Xie, Y., Guo, H., Xu, L., Ge, J., Zhu, Y., Wang, S., Guo, Z., Wang, Z., Duan, H., Zuo, L., and Huang, W.: GlobalRice20: A 20 m resolution global paddy rice dataset for 2015 and 2024 derived from multi-source remote sensing [dataset], https://doi.org/10.5281/zenodo.18168302, 2026.

Zhao, X., Nishina, K., Izumisawa, H., Masutomi, Y., Osako, S., and Yamamoto, S.: Monsoon Asia Rice Calendar (MARC): a gridded rice calendar in monsoon Asia based on Sentinel-1 and Sentinel-2 images, Earth System Science Data, 16, 3893-3911, 2024a.

Zhao, Z., Dong, J., Zhang, G., Yang, J., Liu, R., Wu, B., and Xiao, X.: Improved phenology-based rice mapping algorithm by integrating optical and radar data, Remote Sensing of Environment, 315, 114460, 2024b.